RSC Advances

PAPER

View Article Online
View Journal | View Issue

Cite this: *RSC Adv.*, 2022, **12**, 32480

In situ fabrication of a novel CdS/$ZnIn_2S_4$/g-C_3N_4 ternary heterojunction with enhanced visible-light photocatalytic performance†

Jingzhe Li,[a] Yue Chen,[a] Liezhen Zhu,[a] Linfa Liao,[a] Xinmao Wang,[a] Xun Xu,[a] Lingfang Qiu,[a] Jiangbo Xi,[b] Ping Li*[a] and Shuwang Duo*[a]

Received 8th October 2022
Accepted 8th November 2022

DOI: 10.1039/d2ra06328j

rsc.li/rsc-advances

In this study, a novel g-C_3N_4-based ternary heterojunction was rationally designed and constructed by the *in situ* growth of $ZnIn_2S_4$ nanosheets and CdS nanoparticles onto the g-C_3N_4 nanosheets using a facile two-step oil-bath method. Through optimizing the proportion of $ZnIn_2S_4$ and CdS component, g-C_3N_4 nanosheets coupled with $ZnIn_2S_4$ nanosheets and CdS nanoparticles (denoted as CdS/$ZnIn_2S_4$/g-C_3N_4) exhibited obviously higher photocatalytic properties for RhB removal than the single-component and dual-component systems. Among the as-obtained ternary photocatalysts, it was found that the ternary CdS/$ZnIn_2S_4$/g-C_3N_4-0.2 photocatalyst displayed the optimum photocatalytic property (96%) within a short time (30 min), which was almost 27.42 and 1.17 times higher than that of pure g-C_3N_4 and binary $ZnIn_2S_4$/g-C_3N_4-0.7 composite. The excellent activity of the ternary CdS/$ZnIn_2S_4$/g-C_3N_4 heterostructure is assigned to the synergetic effects of CdS nanoparticles, $ZnIn_2S_4$ nanosheets and g-C_3N_4 nanosheets, which not only broaden the visible-light absorption range, but also improve the charge mobility and separation rate, thus boosting the visible-light-driven photocatalytic property of g-C_3N_4.

1. Introduction

With the rapid development of modern industrialization, environmental pollution, especially water pollution, has become a deadly threat to human health and environmental security due to its long-term harm to human beings and aquatic organisms.[1–3] Traditional techniques such as physical,[4] chemical[5] and biological methods[6] for eliminating residual organic contaminants from water suffer from inefficiency and secondary pollution. Nowadays, photocatalysis, as a green technology, has been widely accepted as a potential alternative method for energy conversion and environmental governance due to its high efficiency and environmentally friendliness.[7–9] Unfortunately, insufficient utilization of visible light restricts the practical application of conventional photocatalysts such as TiO_2 and ZnO.[10,11] Thus, the development of efficient visible-light-responsive photocatalysts is still greatly desired.

In recent years, the use of two-dimensional (2D) metal-free graphite carbon nitride (g-C_3N_4) in the field of visible-light photocatalysis for hydrogen production,[12,13] CO_2 reduction[14,15] and organic pollutants degradation[16,17] has attracted extensive attention owing to its excellent stability and environment friendly preparation process. Nonetheless, the pristine g-C_3N_4 still suffers from poor separation of the photo-induced charge carriers and insufficient absorption of visible light, which severely restrict its actual application.[18,19] Various strategies, such as construction of heterojunctions,[20,21] elements doping,[22,23] and morphologies regulation,[24,25] have been proposed to control and modify g-C_3N_4. Of which, construction of heterojunctions with other narrow-band-gap semiconductors is designated as an effective strategy to overcome the above-mentioned shortcomings of unitary g-C_3N_4.[26,27] Indium zinc sulfide ($ZnIn_2S_4$), as a ternary chalcogenide, has been widely used in the field of photocatalysis owing to wide visible-light response range, excellent photoelectric properties, and remarkable chemical stability.[28,29] More importantly, $ZnIn_2S_4$ possesses an appropriate bandgap structure, which can match well with g-C_3N_4.[30] Actually, the construction of $ZnIn_2S_4$/g-C_3N_4 heterojunction has been proved to be an effective measure to achieve high separation and migration efficiency of photo-generated carriers.[31] Additionally, cadmium sulphide (CdS) is also an attractive candidate to couple with g-C_3N_4 for constructing the heterojunction photocatalyst owing to its excellent

[a]*Jiangxi Key Laboratory of Surface Engineering, School of Materials and Mechanical & Electrical Engineering, Jiangxi Science and Technology Normal University, Nanchang, Jiangxi, 330013, P. R. China. E-mail: lp1849065552@163.com; dsw@jxstnu.edu.cn*

[b]*Key Laboratory of Novel Biomass-Based Environmental and Energy Materials in Petroleum and Chemical Industry, Key Laboratory of Green Chemical Engineering Process of Ministry of Education, Engineering Research Center of Phosphorus Resources Development and Utilization of Ministry of Education, Hubei Key Laboratory of Novel Reactor and Green Chemical Technology, School of Chemistry and Environmental Engineering, Wuhan Institute of Technology, Wuhan, 430073, P. R. China*

† Electronic supplementary information (ESI) available: The XRD patterns of $ZnIn_2S_4$/g-C_3N_4 composites, XPS survey spectrum and EDS element mappings of CdS/$ZnIn_2S_4$/g-C_3N_4-0.2, XRD spectra and SEM image of CdS/$ZnIn_2S_4$/g-C_3N_4-0.2 during a four-cycle experiment. See DOI: https://doi.org/10.1039/d2ra06328j

electronic and structural properties.[32,33] Recently, CdS is widely used as a promoter decorating the main catalyst to further enhance the photocatalytic properties of the ternary heterostructures such as CdS/$ZnIn_2S_4$/TiO_2,[34] CdS-g-C_3N_4-GA[35] and CdS/$Bi_{20}TiO_{32}$/$Bi_4Ti_3O_{12}$.[36] Thus, we expect the introduction of CdS nanoparticles to the binary $ZnIn_2S_4$/g-C_3N_4 heterojunction will further enhance the photocatalytic property of g-C_3N_4.

In this work, we designed and prepared a novel ternary-component CdS/$ZnIn_2S_4$/g-C_3N_4 heterojunction *via* thermal polymerization followed by a two-step *in situ* deposition method. The photocatalytic property of the as-obtained ternary samples was investigated *via* degrading contaminant Rhodamine B (RhB) under visible light irradiation. Owing to the rational construction of ternary composite, CdS/$ZnIn_2S_4$/g-C_3N_4 revealed a faster transfer and separation rate of photo-induced charge carriers as well as a wider visible-light response range compared to that of g-C_3N_4 and $ZnIn_2S_4$/g-C_3N_4-0.7, and thus obtaining obvious higher photocatalytic activity. Finally, the underlying mechanism of CdS/$ZnIn_2S_4$/g-C_3N_4 is elucidated in detail to explain the improvement of the photocatalytic property.

2. Materials and methods

2.1. Materials

All the chemicals were of analytical grade and used without pretreatment. Ethylenediamine tetraacetic acid disodium (EDTA-2Na) and zinc chloride ($ZnCl_2$) were commercially available from Xilong Science Co., Ltd (Guangdong, China). RhB was bought from Aladdin Biochemical Technology Co., Ltd (Shanghai, China). *p*-Benzoquinone (BQ) and tertiary butyl alcohol (*t*-BuOH) were purchased from Shanghai Zhanyun Chemical Co., Ltd (Shanghai, China). Absolute ethanol (EtOH) and hydrochloric acid (HCl) were acquired from Kermel Chemical Reagent Co., Ltd (Tianjin, China). Cadmium chloride hemi (pentahydrate) ($CdCl_2 \cdot 2.5H_2O$) and indium chloride ($InCl_3$) were supplied by Macklin Biochemical Co., Ltd (Shanghai, China). Dicyandiamine (DICY), ammonium chloride (NH_4Cl), and thioacetamide (TAA) were originated from Sinopharm Chemical Reagent Co., Ltd (Shanghai, China). Deionized water was used during the experiments.

2.2. Preparation of g-C_3N_4 nanosheets

The g-C_3N_4 nanosheets were obtained *via* a polymerization process according to the literature.[37] In detail, 3 g of DICY and 15 g of NH_4Cl were transferred into a 100 mL round flask containing 50 mL of deionized water, and then the mixture was heated at 80 °C until completely evaporated. The obtained white powder underwent calcination at 550 °C for 4 h in a muffle furnace under air. Finally, light yellow powder of g-C_3N_4 nanosheets was obtained.

2.3. Synthesis of $ZnIn_2S_4$/g-C_3N_4 binary heterojunctions

The $ZnIn_2S_4$/g-C_3N_4 composites were *in situ* constructed *via* oil-bath heating. Typically, 0.2 g of g-C_3N_4 was dispersed in 50 mL of deionized water (pH = 2.5) by ultrasonic. Then calculated quantity of $ZnCl_2$, $InCl_3$, and TAA were dissolved in the above solution *via* magnetic stirring. After that, the mixture was heated at 80 °C for 2 h. After washed by water and ethanol three times as well as dried at 60 °C overnight, the target product was obtained and labelled as $ZnIn_2S_4$/g-C_3N_4-*X* (*X* presents the weight percent of $ZnIn_2S_4$ and g-C_3N_4). For reference, $ZnIn_2S_4$ was also prepared by same procedure but in the absence of g-C_3N_4.

2.4. Synthesis of CdS/$ZnIn_2S_4$/g-C_3N_4 ternary heterojunctions

The synthesis of ternary CdS/$ZnIn_2S_4$/g-C_3N_4 heterojunctions was performed by another oil-bath heating process. Briefly, 0.015 g of as-obtained $ZnIn_2S_4$/g-C_3N_4-0.7 was first dispersed in 50 mL of deionized water by magnetic stirring, while 0.05 g $CdCl_2 \cdot 2.5H_2O$ and 0.02 g of TAA were dispersed into the above solution. Afterward, the mixture was heated at 70 °C for 2 h. After centrifugation, washing and drying, the target product was collected and labeled as CdS/$ZnIn_2S_4$/g-C_3N_4-*Y* (*Y* presents the weight percent of CdS and $ZnIn_2S_4$/g-C_3N_4). For comparison, CdS, CdS/$ZnIn_2S_4$-0.2, and CdS/g-C_3N_4-0.2 were also prepared by same procedure in the absence of $ZnIn_2S_4$/g-C_3N_4-0.7 and using $ZnIn_2S_4$ or g-C_3N_4 instead of $ZnIn_2S_4$/g-C_3N_4-0.7, respectively. The detailed process utilized to prepare the CdS/$ZnIn_2S_4$/g-C_3N_4 composites is depicted in Scheme 1.

2.5. Characterization

The microstructure and morphologies were investigated by X-ray diffraction (XRD, XRD-6100), X-ray photoelectron spectroscopy (XPS, ESCALAB 250Xi), scanning electron microscopy (SEM, Zeiss Sigma) and transmission electron microscope (TEM, Tecnai G220 S-TWIN). Light absorption property was evaluated by UV-vis diffuse reflectance spectroscopy (UV-vis DRS, UV-2550). Photoluminescence (PL) spectra (excitation at 320 nm) were implemented on a spectrophotometer (ZolixLSP-X500A). The surface specific areas of the samples were measured by N_2 isothermal adsorption–desorption spectroscopy (Autosorb-Iq2, Quantachrome). Photoelectrochemical tests were performed on an electrochemical station (CHI660E) three-electrode cell system using 500 W Xe lamp as light source. The total organic carbon (TOC) measures were performed on a TOC analyser (TOC-2000, Metash). Electron spin resonance (ESR) spectra were acquired using an EMXnano spectrometer (Bruker).

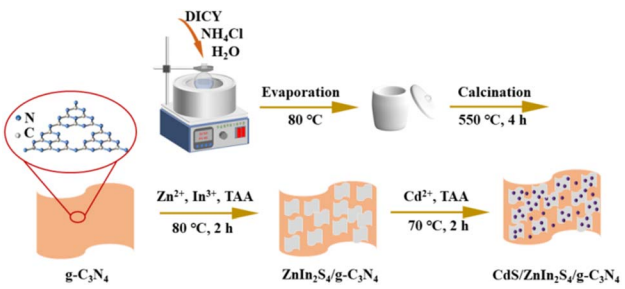

Scheme 1 The formation procedure of CdS/$ZnIn_2S_4$/g-C_3N_4 ternary photocatalysts.

2.6. Evaluation of the photocatalytic activity

The photodegradation properties were evaluated by using RhB as simulated organic pollutants under the visible light irradiation provided by a 500 W Xe lamp with a cutoff filter ($\lambda \geq 420$ nm). Shortly, photocatalysts (20 mg) were dispersed in fresh RhB aqueous solution (50 mL, 50 mg L^{-1}) and stirred for 60 min in a dark environment to realize the saturation adsorption prior to the light irradiation. After given intervals, aliquots (~3 mL) were taken out, filtered by 0.22 μm filter membrane, and traced absorbance change at 554 nm on a UV-vis spectrophotometer (Lambda 35, PerkinElmer). Furthermore, the reusability of CdS/$ZnIn_2S_4$/g-C_3N_4-0.2 was also investigated by recycled photocatalytic experiments.

3. Results and discussion

The purity and crystalline nature of the specimen series were firstly analyzed by XRD. As displayed in Fig. 1 and S1,† the characteristic pattern of the pure g-C_3N_4 are assigned to the graphite-like hexagonal phase, which ascribes well to JCPDS card no. 87-1526.[38] The observed diffraction peaks of pristine $ZnIn_2S_4$ were attributed to hexagonal crystal structure (JCPDS no. 72-0773).[39] The diffraction peaks of bare CdS matched well with reported value by JCPDS no. 77-2306.[40] For the binary $ZnIn_2S_4$/g-C_3N_4, CdS/$ZnIn_2S_4$ or CdS/g-C_3N_4 photocatalysts, the XRD spectra can well indexed to g-C_3N_4 and $ZnIn_2S_4$ or CdS, which reflects the coexistence of two phases. After CdS was further incorporated into $ZnIn_2S_4$/g-C_3N_4-0.7 composite, several typical peaks of CdS appear, revealing that CdS was successfully presented in CdS/$ZnIn_2S_4$/g-C_3N_4 composite. With the increase of $ZnIn_2S_4$ content in the binary $ZnIn_2S_4$/g-C_3N_4 composites (Fig. S1†) and CdS content in the ternary CdS/$ZnIn_2S_4$/g-C_3N_4 composites (Fig. 1), the peak intensity of $ZnIn_2S_4$ and CdS gradually increased, respectively. Simultaneously, it can be seen that the diffraction peak of g-C_3N_4 (002) is appearing at almost same position of the diffraction peaks of $ZnIn_2S_4$ (102), CdS (002), and CdS (101), so as to the peak belonging to g-C_3N_4 is possibly overlapping of the $ZnIn_2S_4$ (102), CdS (002), and CdS (101) peaks, and thus possessing a distinguishable diffraction widening. Besides, no other peaks could be detected in the XRD spectra of single-component, binary-component, and ternary-component photocatalysts, indicating that there are no impurities produced during the synthesis.

The surface chemical composition and valence state of CdS/$ZnIn_2S_4$/g-C_3N_4-0.2 were further evaluated by XPS. As depicted in Fig. S2,† the survey XPS spectrum declared the co-occurrence of Cd, S, Zn, In, S, C and N elements in the ternary sample. In the C 1s spectrum (Fig. 2a), the peaks centered at 288.1 and 284.8 eV could be ascribed to graphitic carbon (C=C) and sp^2-hybridized carbon (N–C=N), respectively.[41] For N 1s (Fig. 2b), the binding energies of peaks at 398.4, 399.5, and 400.7 eV are derived from sp^2-hybridized nitrogen (C–N=C), tertiary nitrogen N–$(C)_3$ groups and amino functions carrying hydrogen (C–N–H), separately.[42] The S 2p XPS regions could be deconvoluted into two peaks at 161.6 eV (S $2p_{3/2}$) and 162.9 eV (S $2p_{1/2}$) seen in Fig. 2c, which implies the existence of S^{2-} ions in the ternary composite.[43] The high-resolution XPS spectrum of Zn 2p (Fig. 2d) displayed two significant peaks located at 1044.7 eV (Zn $2p_{1/2}$) and 1021.6 eV (Zn $2p_{3/2}$), which corresponded to the Zn^{2+} state.[44] The In 3d XPS spectrum shows two characteristic peaks at 444.7 and 452.3 eV, corresponding to In $3d_{5/2}$ and In $3d_{3/2}$ of In^{3+} in $ZnIn_2S_4$ (Fig. 2e).[45] The Cd 3d XPS spectrum reveals two strong peaks at 406.0 (Cd $3d_{5/2}$) and 412.5 eV (Cd $3d_{3/2}$), which are ascribed to the state of Cd^{2+} (Fig. 2f).[46]

The morphology and microstructures of as-obtained photocatalysts were systematically characterized *via* SEM and TEM, and the results are depicted in Fig. 3. Fig. 3a shows the morphology of as-constructed g-C_3N_4 with irregular nanosheets. In Fig. 3b, the pure $ZnIn_2S_4$ with hierarchical flowerlike architecture consisted of thin nanosheets is also successfully constructed *via* a simple oil-bath method. As for $ZnIn_2S_4$/g-C_3N_4-0.7 (Fig. 3c), $ZnIn_2S_4$ nanosheets uniformly disperse on the surface of g-C_3N_4, meaning that a typical 2D/2D heterojunction forms between $ZnIn_2S_4$ and g-C_3N_4. The SEM image (Fig. 3d) of CdS/$ZnIn_2S_4$/g-C_3N_4-0.2 clearly shows a laminated structure consisting of $ZnIn_2S_4$ nanosheets and g-C_3N_4 nanosheets. Nevertheless, CdS nanoparticles cannot be clearly distinguished, which may be ascribed to the small particle size of CdS, the

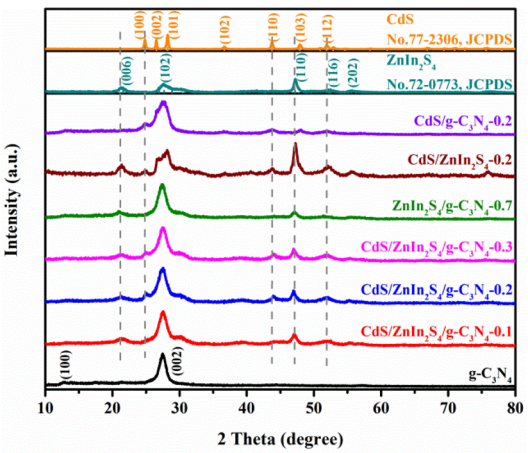

Fig. 1 The XRD patterns of g-C_3N_4, $ZnIn_2S_4$, CdS, CdS/g-C_3N_4-0.2, CdS/$ZnIn_2S_4$-0.2, $ZnIn_2S_4$/g-C_3N_4-0.7 and CdS/$ZnIn_2S_4$/g-C_3N_4-*Y* (*Y* = 0.1, 0.2 and 0.3).

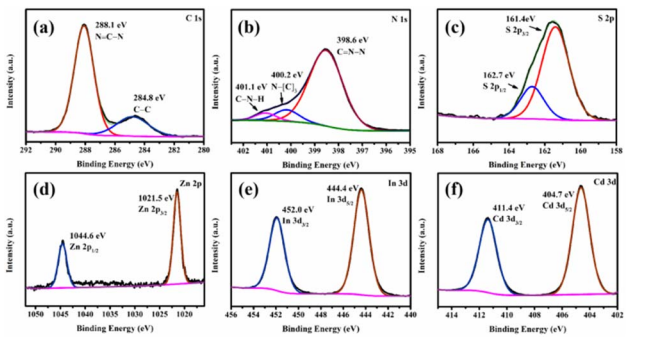

Fig. 2 The XPS spectra of CdS/$ZnIn_2S_4$/g-C_3N_4-0.2: C 1s (a), N 1s (b), S 2p (c), Zn 2p (d), In 3d (e), and Cd 3d (f).

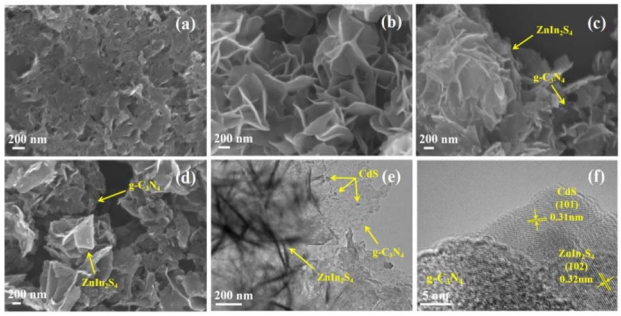

Fig. 3 SEM images of g-C_3N_4 (a), $ZnIn_2S_4$ (b), $ZnIn_2S_4$/g-C_3N_4-0.7 (c), and CdS/$ZnIn_2S_4$/g-C_3N_4-0.2 (d); TEM (e) and HR-TEM (f) images of CdS/$ZnIn_2S_4$/g-C_3N_4-0.2.

corresponding energy-dispersive system (EDS) element mappings (Fig. S3†) indicate the simultaneous existence and even distribution of g-C_3N_4, $ZnIn_2S_4$, and CdS. Fig. 3e shows the TEM image of CdS/$ZnIn_2S_4$/g-C_3N_4-0.2 heterojunction, which consists of g-C_3N_4 nanosheets, $ZnIn_2S_4$ nanosheets, and CdS nanoparticles. High resolution TEM (HR-TEM) image (Fig. 3f) displays the lattice fringes space of 0.32 and 0.31 nm corresponded to the (102) plane of $ZnIn_2S_4$ and (101) plane of CdS, separately.[47,48] These results further confirm the successful construction of target product.

Commonly, large specific surface areas may provide abundant surface active sites for the absorption of reactant molecules, and thus boosting the photocatalytic property.[49] Thereby, the specific surface area and pore volume distribution of g-C_3N_4, $ZnIn_2S_4$/g-C_3N_4-0.7, and CdS/$ZnIn_2S_4$/g-C_3N_4-0.2 were investigated by N_2 adsorption method. As displayed in Fig. 4a, all three samples show the classical type IV isotherms with the type H_3 hysteresis loops, indicating the existence of mesoporous structure.[50] The specific surface area (Fig. 4a, inset) of pristine g-C_3N_4 is 25.186 $m^2\ g^{-1}$. After successively coupling with $ZnIn_2S_4$ and CdS, the specific surface area of g-C_3N_4 increases from 25.186 $m^2\ g^{-1}$ to 40.944 and 49.175 $m^2\ g^{-1}$, which suggests that $ZnIn_2S_4$ and CdS can obviously improve the BET surface area of g-C_3N_4 providing more active sites for photocatalysis. Moreover, the pore size distributions are displayed in Fig. 4b, the results show that the pore sizes (Fig. 4b, inset) of all three samples distribute at 2–10 nm, which further confirm the presence of mesopores, the mesoporous characteristics are beneficial for producing high surface areas.

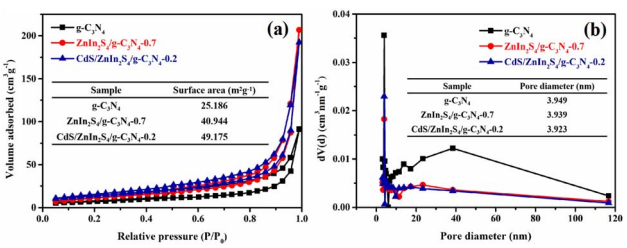

Fig. 4 N_2 adsorption–desorption isotherms (a) and the corresponding pore size distribution plots (b) of g-C_3N_4, $ZnIn_2S_4$/g-C_3N_4-0.7 and CdS/$ZnIn_2S_4$/g-C_3N_4-0.2.

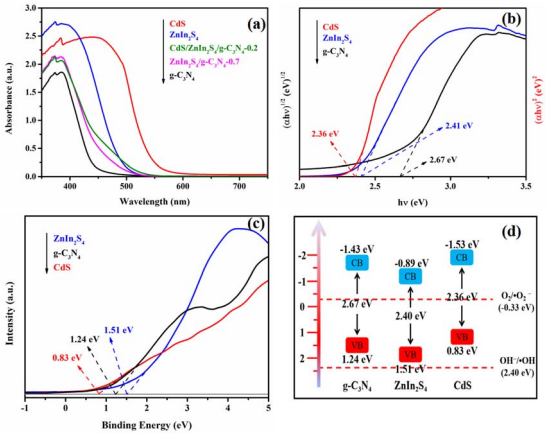

Fig. 5 UV-vis DRS of g-C_3N_4, $ZnIn_2S_4$, CdS, $ZnIn_2S_4$/g-C_3N_4-0.7 and CdS/$ZnIn_2S_4$/g-C_3N_4-0.2 (a); the band gap (b), VB-XPS (c), and energy band structure (d) of g-C_3N_4, $ZnIn_2S_4$, CdS.

The light absorption capacity of the g-C_3N_4, $ZnIn_2S_4$, CdS, $ZnIn_2S_4$/g-C_3N_4-0.7 and CdS/$ZnIn_2S_4$/g-C_3N_4-0.2 photocatalysts was investigated by UV-vis DRS, and the related results are depicted in Fig. 5. Based on the results displayed in Fig. 5a, the light absorption thresholds of g-C_3N_4, $ZnIn_2S_4$, and CdS are approximately 446 and 500, 562 nm, separately, which are basically in accord with the previous reports.[51,52] After *in situ* growing $ZnIn_2S_4$ and CdS on g-C_3N_4, the light absorption threshold of the $ZnIn_2S_4$/g-C_3N_4-0.7 and CdS/$ZnIn_2S_4$/g-C_3N_4-0.2 heterojunctions have significant red shifts, indicating that the combination of $ZnIn_2S_4$ and CdS can effectively widen the light absorption range of g-C_3N_4. The wider the light absorption range, the more conducive it is to utilize visible light, which is more beneficial to enhance the photocatalytic performance. Fig. 5b shows the bandgap energies (E_g) of g-C_3N_4, $ZnIn_2S_4$, and CdS estimated by Tauc plot method,[53] which are 2.67, 2.40 and 2.36 eV, separately. To further obtain the band edges of g-C_3N_4, $ZnIn_2S_4$, and CdS, their valence band XPS spectra (VB-XPS) were further measured. According to the VB-XPS results depicted in Fig. 5c, the valence band (VB) potentials of g-C_3N_4, $ZnIn_2S_4$, and CdS are 1.24, 1.51, and 0.83 eV, separately. E_g and edge potentials of VB and conduction band (CB) possess the relationship: $E_g = E_{VB} - E_{CB}$. As a result, the CB potentials of g-C_3N_4, $ZnIn_2S_4$, and CdS can be determined as −1.43, −0.89, and −1.53 eV, separately. Accordingly, the overall band structure positions of g-C_3N_4, $ZnIn_2S_4$, and CdS can be obtained and the results are shown in Fig. 5d.

The internal electron transfer behaviors of photo-induced charge carrier were firstly analyzed by PL technique. As we all know, a lower PL signal represents a higher separation efficiency of photo-generated charge carrier.[54] As illustrated in Fig. 6a, intense emission peak near 450 nm can be observed for the pristine g-C_3N_4, indicating an inherent nature of a low separation rate. In contrast, the PL intensity of the $ZnIn_2S_4$/g-C_3N_4-0.7 and heterojunction obviously quenched. After further coupling with CdS, the obtained CdS/$ZnIn_2S_4$/g-C_3N_4-0.2 ternary heterojunction displays a lower PL signal, indicating that the charge

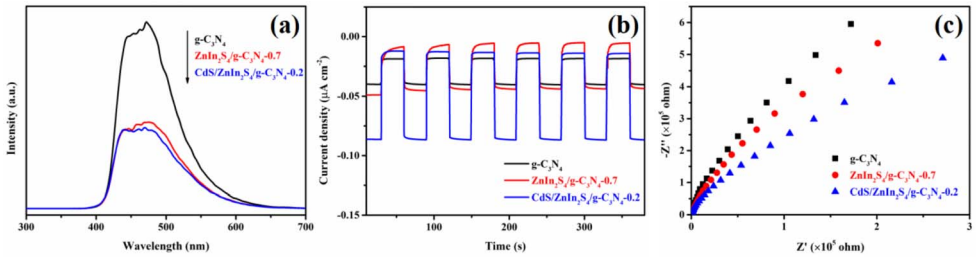

Fig. 6 PL spectra (a), transient photocurrent responses (b), and Nyquist plots (c) of g-C_3N_4, $ZnIn_2S_4$/g-C_3N_4-0.7 and CdS/$ZnIn_2S_4$/g-C_3N_4-0.2.

carriers' separation efficiency of g-C_3N_4 can be accelerated by forming ternary heterojunction with $ZnIn_2S_4$ and CdS. To verify this result, photelectrochemical measurements were performed to support the improved separation and transfer efficiency. Generally, higher photocurrent intensity or smaller semicircle radius means higher separation and transfer efficiency of photo-generated charge carriers.[55] As displayed in Fig. 6b, the photocurrent intensity of CdS/$ZnIn_2S_4$/g-C_3N_4-0.2 composite is obviously higher that of $ZnIn_2S_4$/g-C_3N_4-0.7 and g-C_3N_4. The results of electrochemical impedance spectroscopy (EIS) (Fig. 6c) show CdS/$ZnIn_2S_4$/g-C_3N_4-0.2 possesses the lowest charge transfer impedance due to its smaller semicircle radius than the two other samples. The photoelectrochemical results forcefully verify that the constructing of CdS/$ZnIn_2S_4$/g-C_3N_4-0.2 ternary composite significantly promotes the charge carrier transfer and separation, and thus delivering boosting photocatalytic property.

The visible-light photocatalytic activities of the pristine g-C_3N_4, $ZnIn_2S_4$, CdS, CdS/g-C_3N_4-0.2, CdS/$ZnIn_2S_4$-0.2, and a series of $ZnIn_2S_4$/g-C_3N_4 and CdS/$ZnIn_2S_4$/g-C_3N_4 composites were evaluated by the degradation of RhB. As depicted in Fig. 7a, the degradation efficiency of $ZnIn_2S_4$ and CdS is obviously higher than that of g-C_3N_4 due to their wider visible-light response range. The photocatalytic properties of g-C_3N_4 and $ZnIn_2S_4$ are obviously improved after coupling with $ZnIn_2S_4$ or CdS. Among of the $ZnIn_2S_4$/g-C_3N_4 composites, $ZnIn_2S_4$/g-C_3N_4-0.2 exhibited the highest degradation efficiency of 82% within 30 min. When $ZnIn_2S_4$/g-C_3N_4-0.2 further coupled with CdS, the photocatalytic activities could be obviously improved. Among the ternary photocatalysts, CdS/$ZnIn_2S_4$/g-C_3N_4-0.7 exhibited the highest degradation efficiency, in which 96% of RhB could be degradated within 30 min. Moreover, the photocatalytic kinetics of RhB degradation were evaluated using the psedo-first-order model (Fig. 7b). The CdS/$ZnIn_2S_4$/g-C_3N_4-0.2 showed the highest apparent rate constant, approximately 0.10868 min^{-1}, which is far greater than that of the pristine g-C_3N_4 (0.00043 min^{-1}), $ZnIn_2S_4$/g-C_3N_4-0.7 (0.05475 min^{-1}) and CdS/g-C_3N_4-0.2 (0.02580 min^{-1}) under the same conditions, separately. Furthermore, the TOC measurements were also carried out to investigate the mineralization abilities of photocatalysts under 30 min of visible light irradiation. As illustrated in Fig. 7c, the TOC removal efficiency of CdS/$ZnIn_2S_4$/g-C_3N_4-0.2 (84.65%) is obviously higher than that of g-C_3N_4 (0.40%) and $ZnIn_2S_4$/g-C_3N_4-0.7 (73.97%), which is coincident with the trend of photodegradation performance. This result fully confirms the high mineralization ability of CdS/$ZnIn_2S_4$/g-C_3N_4-0.2 for RhB. The stability is a crucial factor affecting the actual application of the photocatalyst,[56] and thus sequential cycling experiments were performed to detect the stability of the CdS/$ZnIn_2S_4$/g-C_3N_4-0.2 ternary photocatalyst. As displayed in Fig. 7d, the photocatalytic efficiency had no obvious change after four reused tests. Besides, the structure and morphology can also be preserved after undergoing four runs of photodegradation reaction as no noticeable change can be observed in the XRD pattern (Fig. S4†) and SEM image (Fig. S5†). The results prove that the as-prepared ternary catalysts can meet the practical application requirements.

To expound the photocatalytic mechanism of the photocatalytic activity improvement of CdS/$ZnIn_2S_4$/g-C_3N_4 photocatalysts, the predominant active species formed during the photocatalytic process were distinguished *via* a series of trapping experiments over CdS/$ZnIn_2S_4$/g-C_3N_4-0.2. In the experiments, EDTA-2Na, BQ, and *t*-BuOH were chosen as the scavengers of hydroxyl radicals ($^{\bullet}OH$), radical superoxide ($^{\bullet}O_2^-$), and hole (h^+), separately. Fig. 8a exhibits the addition of BQ has a significant effect on the degradation activity, which mean that $^{\bullet}O_2^-$ was the primary active substance during the photocatalytic process. However, after adding EDTA-2Na and *t*-BuOH, the

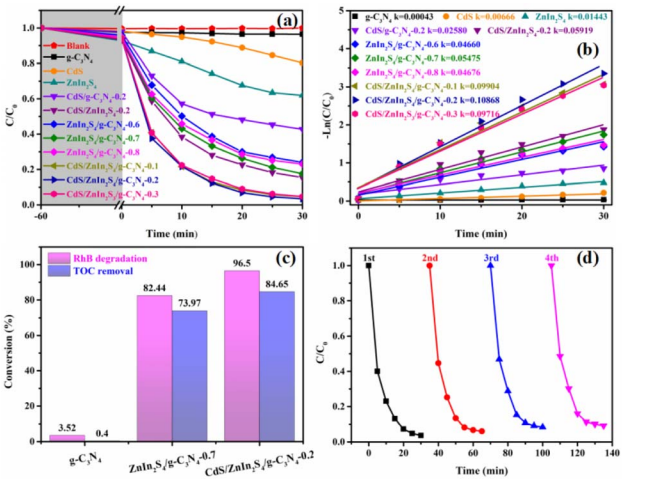

Fig. 7 Visible-light photodegradation of RhB over as-obtained samples (a) and the corresponding kinetics (b); removal rate of TOC by g-C_3N_4, $ZnIn_2S_4$/g-C_3N_4-0.7, and CdS/$ZnIn_2S_4$/g-C_3N_4-0.2 for RhB degradation (c); four cycling tests of photocatalytic degradation RhB for CdS/$ZnIn_2S_4$/g-C_3N_4-0.2 (d).

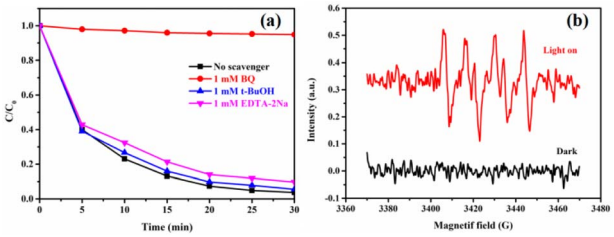

Fig. 8 Photodegradation of RhB over the CdS/$ZnIn_2S_4$/g-C_3N_4-0.2 photocatalyst in the presence of different radical scavengers (a); ESR detection of $^{\bullet}O_2^-$ over CdS/$ZnIn_2S_4$/g-C_3N_4-0.2 (b).

removal efficiency of RhB decreased from 96% to 90% and 94%, separately, which revealed that h^+ had a weak effect on the photocatalytic reaction, while the role of $^{\bullet}OH$ could be ignored owing to the negligible effect of EDTA-2Na on the RhB removal efficiency. Consequently, it could be inferred that the active species played a different role during the photocatalytic reaction process with a sequence of $^{\bullet}O_2^- > h^+ > {}^{\bullet}OH$. In addition, the ESR results (Fig. 8b) provided a persuasive proof for the existence of $^{\bullet}O_2^-$ in the photodegradation reaction. No ESR signals were observed under dark, while the signals of the DMPO-$^{\bullet}O_2^-$ adducts (intensity ratio of 1 : 1 : 1 : 1) could be easily identified after irradiating by visible light, which is fully in accord with the results of radical trapping experiments.

Based on the conclusions above, a plausible photocatalytic charge-transfer mechanism of the CdS/$ZnIn_2S_4$/g-C_3N_4 composite for photocatalytic degradation of RhB is put forward and displayed in Scheme 2. Under the visible light irradiation, g-C_3N_4, $ZnIn_2S_4$ and CdS can adsorb photons and generate a great deal of photo-induced electrons (e^-) and h^+ pairs, where the e^- and h^+ gather at CB and VB, separately. According to the calculated band structure and close contact interface, e^- in the CB of CdS can readily migrate to the CB of $ZnIn_2S_4$ by a one-step process or two-step process. Meanwhile, h^+ in the VB of $ZnIn_2S_4$ transfers to the VB of CdS under the driving force of potential difference. Then, the accumulated e^- in $ZnIn_2S_4$ will react with dissolved O_2 to produce $^{\bullet}O_2^-$ due to its more negative potential than $O_2/^{\bullet}O_2^-$ (−0.33 eV *versus* NHE),[57] while the VB potential of CdS is too low for h^+ to convert –OH into $^{\bullet}OH$ (+2.4 eV *versus* NHE).[58] Finally, the $^{\bullet}O_2^-$ and h^+ behave as oxidation active site for the degradation of RhB due to their high oxidative capacity.

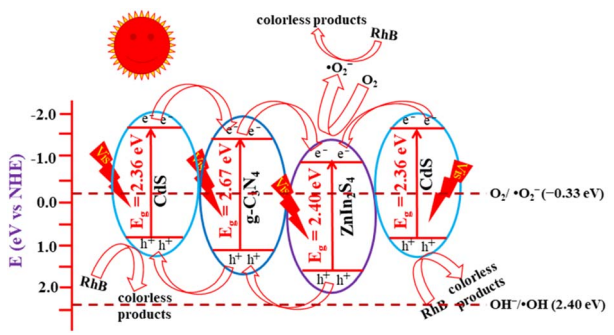

Scheme 2 Proposed mechanism for the visible-light photodegradation of RhB over CdS/$ZnIn_2S_4$/g-C_3N_4 ternary composite.

4 Conclusions

In general, the CdS/$ZnIn_2S_4$/g-C_3N_4 ternary photocatalyst was prepared by a facile pyrolysis route coupling with simple two-step oil-bath procedure and the photoactivity was evaluated by degrading RhB under visible light irradiation. As expected, CdS/$ZnIn_2S_4$/g-C_3N_4 ternary composites possess boosted photocatalytic performance, which is not only higher than bare g-C_3N_4, $ZnIn_2S_4$ and CdS, but also even superior to $ZnIn_2S_4$/g-C_3N_4 and CdS/g-C_3N_4 binary photocatalysts. Among them, the CdS/$ZnIn_2S_4$/g-C_3N_4-0.2 photocatalyst achieves the best photocatalytic activity with a degradation rate of 96%. Additionally, the proposed CdS/$ZnIn_2S_4$/g-C_3N_4-0.2 composite reveals excellent photostability and reusability after four reused tests. The reasonable construction of ternary heterojunction not only facilitates the photogenerated charge carrier separation and migration as well as widen the visible-light response range, but also enhances the specific surface area, all of which are favorable for photocatalytic process. The design and fabrication of the CdS/$ZnIn_2S_4$/g-C_3N_4 ternary heterojunction photocatalysts represent a promising approach to fabricate high efficient g-C_3N_4-based photocatalysts for environmental remediation.

Author contributions

Jingzhe Li: data curation, investigation, writing – original draft. Yue Chen and Liezhen Zhu: investigation, validation, data curation. Linfa Liao and Xinmao Wang: investigation, validation. Xun Xu and Lingfang Qiu: conceptualization, funding acquisition, supervision. Jiangbo Xi: investigation, methodology. Ping Li: conceptualization, methodology, funding acquisition, writing – review & editing, supervision. Shuwang Duo: conceptualization, funding acquisition, project administration, supervision.

Conflicts of interest

There are no conflicts to declare.

Acknowledgements

This work was supported by the National Natural Science Foundation of China (No. 41763020), the Natural Science Foundation of Jiangxi Province (No. 20212BAB204020, 20202BABL214040, and 20202BABL213014), and the Postgraduate Innovation Special Fund Project of Jiangxi Provincial Education Department (YC2022-s779).

Notes and references

1 J. B. Xi, Q. J. Wang, X. M. Duan, N. Zhang, J. X. Yu, H. Y. Sun and S. Wang, *Chem. Eng. Sci.*, 2021, **231**, 116303.
2 B. S. Li, C. Lai, L. Qin, C. C. Chu, M. M. Zhang, S. Y. Liu, X. G. Liu, H. Yi, J. F. He, L. Li, M. F. Li and L. Chen, *J. Colloid Interface Sci.*, 2020, **560**, 701–713.

3 J. Wang, G. Wang, B. Cheng, J. Yu and J. Fan, *Chin. J. Catal.*, 2021, **42**, 56–68.
4 M. T. Islam, R. Saenz-Arana, C. Hernandez, T. Guinto, M. A. Ahsan, D. T. Bragg, H. Y. Wang, B. Alvarado-Tenorio and J. C. Noveron, *J. Environ. Chem. Eng.*, 2018, **6**, 3070–3082.
5 T. Luo, H. P. Feng, L. Tang, Y. Lu, W. W. Tang, S. Chen, J. F. Yu, Q. Q. Xie, X. Ouyang and Z. M. Chen, *Chem. Eng. J.*, 2020, **382**, 122970.
6 X. Yang, G. R. Xu, H. R. Yu and Z. Zhang, *Bioresour. Technol.*, 2016, **211**, 566–573.
7 X. Gong, X. G. Ma, F. D. Wan, W. Y. Duan, X. L. Yang and J. R. Zhu, *Acta Chim. Sin.*, 2022, **80**, 510–516.
8 Z. Y. Zhang, X. L. Xue and X. Y. Chen, *Dalton Trans.*, 2022, **51**, 8015–8027.
9 T. Y. Zhao, Z. P. Xing, Z. Y. Xiu, Z. Z. Li, S. L. Yang, Q. Zhu and W. Zhou, *Int. J. Hydrogen Energy*, 2019, **44**, 1586–1596.
10 H. Liu, J. Z. Li, P. Li, G. Z. Zhang, X. Xu, H. Zhang, L. F. Qiu, H. Qi and S. W. Duo, *Acta Chim. Sin.*, 2021, **79**, 1293–1301.
11 P. Molaei and F. R. Moghadam, *Mater. Today Commun.*, 2022, **31**, 103677.
12 J. W. Fu, Q. L. Xu, J. X. Low, C. J. Jiang and J. G. Yu, *Appl. Catal., B*, 2019, **243**, 556–565.
13 H. C. Yang, R. Y. Cao, P. X. Sun, J. M. Yin, S. W. Zhang and X. J. Xu, *Appl. Catal., B*, 2019, **256**, 117862.
14 Y. Huo, J. F. Zhang, K. Dai and C. H. Liang, *ACS Appl. Energy Mater.*, 2021, **4**, 956–968.
15 C. Yang, Q. Y. Tan, Q. Li, J. Zhou, J. J. Fan, B. Li, J. Sun and K. L. Lv, *Appl. Catal., B*, 2020, **268**, 118738.
16 Q. H. Shen, C. Y. Wu, Z. Y. You, F. L. Huang, J. S. Sheng, F. Zhang, D. Cheng and H. Yang, *J. Mater. Res.*, 2020, **35**, 2148–2157.
17 Y. C. Wang, J. Zhou, X. Q. Hao, Y. Wang and Z. G. Zou, *Appl. Surf. Sci.*, 2018, **456**, 861–870.
18 Y. C. Deng, J. Liu, Y. B. Huang, M. M. Ma, K. Liu, X. M. Dou, Z. J. Wang, S. C. Qu and Z. G. Wang, *Adv. Funct. Mater.*, 2020, **30**, 2002353.
19 C. Zhang, D. Y. Qin, Y. Zhou, F. Z. Qin, H. Wang, W. J. Wang, Y. Yang and G. M. Zeng, *Appl. Catal., B*, 2022, **303**, 120904.
20 X. Zhu, Y. T. Wang, Y. Guo, J. Z. Wan, Y. Yan, Y. X. Zhou and C. Sun, *Appl. Surf. Sci.*, 2021, **544**, 148872.
21 B. Zhang, X. Y. Hu, E. Z. Liu and J. Fan, *Chin. J. Catal.*, 2021, **42**, 1519–1529.
22 S. H. Wang, J. W. Zhan, K. Chen, A. Ali, L. H. Zeng, H. Zhao, W. L. Hu, L. X. Zhu and X. L. Xu, *ACS Sustainable Chem. Eng.*, 2020, **8**, 8214–8222.
23 G. M. Liu, G. H. Dong, Y. B. Zeng and C. Y. Wang, *Chin. J. Catal.*, 2020, **41**, 1564–1572.
24 F. He, Z. X. Wang, Y. X. Li, S. Q. Peng and B. Liu, *Appl. Catal., B*, 2020, **269**, 118828.
25 X. Y. Zhang, X. Y. Wang, J. Q. Meng, Y. Q. Liu, M. Ren, Y. H. Guo and Y. X. Yang, *Sep. Purif. Technol.*, 2021, **255**, 117693.
26 B. Zhang, H. X. Shi, Y. J. Yan, C. Q. Liu, X. Y. Hu, E. Z. Liu and J. Fan, *Colloids Surfaces, A*, 2021, **608**, 125598.
27 W. L. Shi, M. Y. Li, X. L. Huang, H. J. Ren, C. Yan and F. Guo, *Chem. Eng. J.*, 2020, **382**, 122960.
28 L. Ye, Z. H. Wen, Z. H. Li and H. T. Huang, *Solar RRL*, 2020, **4**, 2000027.
29 F. H. Mu, Q. Cai, H. Hu, J. Wang, Y. Wang, S. J. Zhou and Y. Kong, *Chem. Eng. J.*, 2020, **384**, 123352.
30 L. L. Li, D. K. Ma, Q. L. Xu and S. M. Huang, *Chem. Eng. J.*, 2022, **437**, 135153.
31 X. M. Liu, S. Q. Wang, F. Yang, Y. C. Zhang, L. S. Yan, K. X. Li, H. Q. Guo, J. J. Yan and J. Lin, *Int. J. Hydrogen Energy*, 2022, **47**, 2900–2913.
32 D. D. Ren, W. N. Zhang, Y. N. Ding, R. C. Shen, Z. M. Jiang, X. Y. Lu and X. Li, *Solar RRL*, 2019, **4**, 1900423.
33 L. Chen, Y. M. Xu and B. L. Chen, *Appl. Catal., B*, 2019, **256**, 117848.
34 H. Liu, J. Z. Li, Y. Chen, X. T. Sun, X. Xu, L. F. Qiu, S. W. Duo and P. Li, *New J. Chem.*, 2022, **46**, 7195–7201.
35 J. H. Liu, X. N. Wei, W. Q. Sun, X. X. Guan, X. C. Zheng and J. Li, *Environ. Res.*, 2021, **197**, 111136.
36 K. Das, R. Bariki, D. Majhi, A. Mishra, K. K. Das, R. Dhiman and B. G. Mishra, *Appl. Catal., B*, 2022, **303**, 120902.
37 M. M. Zhang, C. Lai, B. S. Li, D. L. Huang, G. M. Zeng, P. Xu, L. Qin, S. Y. Liu, X. G. Liu, H. Yi, M. F. Li, C. C. Chu and Z. Chen, *J. Catal.*, 2019, **369**, 469–481.
38 H. G. Yu, H. Q. Ma, X. H. Wu, X. F. Wang, J. J. Fan and J. G. Yu, *Solar RRL*, 2020, **5**, 2000372.
39 F. Min, Z. Q. Wei, Z. Yu, Y. T. Xiao, S. E. Guo, R. J. Song and J. H. Li, *Dalton Trans.*, 2022, **51**, 2323–2330.
40 S. W. Sun, H. Cheng, K. Cao, A. Y. Song, C. Q. Xu, J. X. Ba, H. W. Lin, W. C. Qiu, Z. H. Li, D. H. Fan, J. Huang and S. Y. Jin, *Energy Fuels*, 2022, **36**, 2034–2043.
41 J. F. Zheng, Z. Xu, S. T. Xin, B. C. Zhu and L. H. Nie, *Dalton Trans.*, 2022, **51**, 12883–12894.
42 X. Chang, Y. Wang, X. J. Zhou, Y. Song and M. Y. Zhang, *Dalton Trans.*, 2021, **50**, 17618–17624.
43 J. Chen, K. Li, X. Y. Cai, Y. L. Zhao, X. Q. Gu and L. Mao, *Mater. Sci. Semicond. Process.*, 2022, **143**, 106547.
44 H. Q. Wang, H. P. Jiang, H. J. Wang, Q. Liu and P. W. Huo, *Energy Technol.*, 2022, **10**, 2101158.
45 Y. Gao, K. Qian, B. T. Xu, F. Ding, V. Dragutan, I. Dragutan, Y. G. Sun and Z. H. Xu, *RSC Adv.*, 2020, **10**, 32652–32661.
46 F. Zhang, H. Q. Zhuang, W. M. Zhang, J. Yin, F. H. Cao and Y. X. Pan, *Catal. Today*, 2019, **330**, 203–208.
47 W. Chen, R. Q. Yan, G. H. Chen, M. Y. Chen, G. B. Huang and X. H. Liu, *Ceram. Int.*, 2019, **45**, 1803–1811.
48 Q. L. Yu, G. Z. Wu, T. Zhang, X. D. Zhao, Z. Zhou, L. Liu, W. Chen and P. J. J. Alvarez, *Chem. Commun.*, 2020, **56**, 7613–7616.
49 R. H. Zha, T. Shi, L. He, X. Y. Sun, Y. F. Jia and M. Zhang, *Dyes Pigm.*, 2020, **180**, 108439.
50 L. F. Cui, Y. F. Liu, X. Y. Fang, C. C. Yin, S. S. Li, D. Sun and S. F. Kang, *Green Chem.*, 2018, **20**, 1354–1361.
51 X. Deng, D. D. Wang, H. J. Li, W. Jiang, T. Y. Zhou, Y. Wen, B. Yu, G. B. Che and L. Wang, *J. Alloys Compd.*, 2022, **894**, 162209.
52 G. M. Li, B. Wang, J. Zhang, R. Wang and H. L. Liu, *Appl. Surf. Sci.*, 2019, **478**, 1056–1064.
53 J. F. Jing, J. Yang, W. L. Li, Z. H. Wu and Y. F. Zhu, *Adv. Mater.*, 2022, **34**, 2106807.

54 W. K. Wei, Q. F. Tian, H. S. Sun, P. Liu, Y. Zheng, M. Z. Fan and J. D. Zhuang, *Appl. Catal., B*, 2020, **260**, 118153.
55 R. Arcas, E. Peris, E. Mas-Marzá and F. Fabregat-Santiago, *Sustainable Energy Fuels*, 2021, **5**, 956–962.
56 H. Y. Zhang, B. G. Xu, X. Zhang and P. Yang, *Environ. Sci.: Nano*, 2022, **9**, 3397–3406.
57 J. W. Ren, Y. Meng, X. Zhang, Y. Gao, L. X. Liu, X. X. Zhou, Z. G. Zhang, L. B. Zeng and J. Ke, *Sep. Purif. Technol.*, 2022, **296**, 121423.
58 J. L. Wang, X. Liu, C. S. Li, M. Yuan, B. J. Zhang, J. H. Zhu and Y. Q. Ma, *J. Photochem. Photobiol., A*, 2020, **401**, 112795.